Probing ultrafast carrier tunneling dynamics in individual quantum dots and molecules

Kai Müller[1], Alexander Bechtold[1], Claudia Ruppert[2], Timo Kaldewey[1], Markus Zecherle[1], Johannes S. Wildmann[1], Max Bichler[1], Hubert J. Krenner[3], José M. Villas-Bôas[4], Gerhard Abstreiter[1], Markus Betz[2], and Jonathan J. Finley[1,]*

Ultrafast pump-probe spectroscopy is employed to directly monitor the tunneling of charge carriers from single and vertically coupled quantum dots and probe intra-molecular dynamics. Immediately after resonant optical excitation, several peaks are observed in the pump-probe spectrum arising from Coulomb interactions between the photogenerated charge carriers. The influence of few-Fermion interactions in the photoexcited system and the temporal evolution of the optical response is directly probed in the time domain. In addition, the tunneling times for electrons and holes from the QD nanostructure are independently determined. In polarization resolved measurements, near perfect Pauli-spin blockade is observed in the spin-selective absorption spectrum as well as stimulated emission. While electron and hole tunneling from single quantum dots is shown to be well explained by the WKB formalism, for coupled quantum dots pronounced resonances in the electron tunneling rate are observed arising from elastic and inelastic electron tunneling between the different dots.

1 Introduction

Tunneling of charge carriers underpins a wide range of phenomenology in solid state physics. For example, tunneling of Cooper pairs through insulating Josephson junctions governs the operation of superconducting qubits [1] and is integral to the operation of electronic [2] and magneto-resistive devices [3]. In semiconductors, tunneling barriers have historically been used to tailor the electrical transport properties through the effective potential in heterostructures and exploit quantum effects [4]. Such applications range from the paradigm of the Esaki-Tsu tunneling diode [5] to optimized charge injectors and extractors in quantum cascade lasers [6] and to the operation of spin quantum bits in electrostatically defined quantum dots [7]. In all those situations, tunneling generally occurs from, and to a continuum of electronic states associated with particles moving freely in one or more directions. In contrast, in zero-dimensional nanostructures such as self-assembled quantum dots (QDs) the energy spectrum of electrons and holes is fully quantized. As a result, tunneling out of the quantum dot occurs from a discrete level facilitating the study and utilization of novel phenomena such as Fano [8, 9] and many body physics in tunable solid states systems [10]. It is also possible to design more sophisticated assemblies such as quantum dot molecules (QDMs) [11] where fully quantized energy levels experience a tunnel coupling adjustable by growth parameters and additional external electric fields [12–14]. Such stacked devices permit the direct investigation of carrier tunneling and relaxation dynamics between discrete quantum states with a tunable energy spacing. In this case, relaxation or tunneling requires additional quasiparticles such as phonons to ensure energy conservation and the coupling of the discrete levels to the vibrational spectrum reveals some rich physics [15, 16]. To date, such inelastic tunneling events have only been studied indirectly in transport

* Corresponding author E-mail: finley@wsi.tum.de
[1] Walter Schottky Institut and Physik-Department, Technische Universität München, Am Coulombwall 4, 85748 Garching, Germany
[2] Experimentelle Physik 2, TU Dortmund, 44221 Dortmund, Germany
[3] Lehrstuhl für Experimentalphysik 1 and Augsburg Centre for Innovative Technologies (ACIT), Universität Augsburg, Universitätsstr. 1, 86159 Augsburg, Germany
[4] Instituto de Física, Universidade Federal de Uberlândia, 38400-902 Uberlândia, MG, Brazil

experiments performed on electrostatically defined quantum dots [17, 18] or locally gated nanotubes [19]. In contrast, self-assembled nanostructures offer the convenience of ultrafast optical carrier preparation [20–24] and time-resolved detection of their few-Fermion occupation [20, 22]. As such they present an ideal testbed to directly study elastic as well as inelastic tunneling phenomena associated with discrete solid state quantum levels.

In this paper we report the investigation of ultrafast evolution of the linear optical response of single and vertically coupled quantum dots due to Coulomb interactions and carrier tunneling. Picosecond pump-probe spectroscopy is employed to monitor the evolution of the optical response of the system over the first few hundred picoseconds after an exciton has been resonantly created. Immediately after excitation, a number of pronounced features appear in the transient absorption spectrum due to pump-induced absorption and the resulting few-Fermion interactions in the system. By monitoring the temporal evolution of the pump-probe spectrum we independently track both electron and hole dynamics. For single QDs we demonstrate that the applied electric field dependent tunneling times can be well described by the WKB approximation. For quantum dot molecules with coupled and electrically tunable quantum states we observe ultrafast elastic and inelastic tunneling as the discrete electronic orbitals in each dot are tuned close to energetic resonance. This finding is presented for four different couplings between different excited orbital electron states of the lower dot and one particular orbital state in the upper dot. In polarization resolved pump-probe spectroscopy we observe a near perfect Pauli spin blockade of strongly spin selective transitions as well as spin-selective stimulated emission from the dots.

2 Sample structure and experimental setup

The samples investigated consist of single or vertically stacked pairs of self-assembled InGaAs quantum dots embedded within the intrinsic region of a GaAs Schottky photodiode as depicted schematically in Figure 1a. The figure shows a cross-sectional view of the sample structure consisting of a GaAs substrate, an n-doped GaAs contact layer, a 250–400 nm thick intrinsic GaAs region into which single or double layer of QDs are embedded, and a Ti:Au Schottky front contact. Such devices facilitate complementary photocurrent absorption (PC) and photoluminescence emission (PL) measurements as a function of the the internal electric field (F) [25]. For small

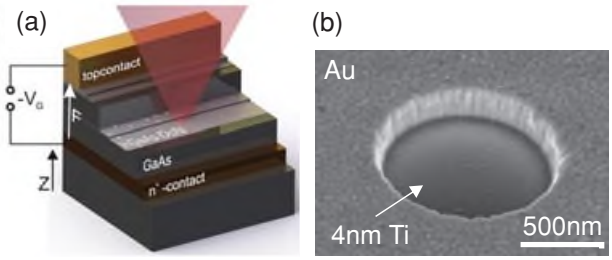

Figure 1 (online color at: www.ann-phys.org) Sample structure: self-assembled InGaAs quantum dots, or quantum dot molecules, embedded within the intrinsic region of an n-i-Schottky diode. (a) Schematic cross-sectional view of the layer structure showing the typical epitaxial layers. (b) SEM image of a 1 μm diameter shadowmask aperture fabricated by deposition of polystyrene nanospheres before the evaporation of an opaque gold layer.

electric fields ($F < 25$ kV/cm) and low temperatures, optical recombination dominates the relaxation of charge carriers localized in the QD nanostructure. In contrast, for large reverse voltages the electric field becomes larger and tunneling out of the QD nanostructure occurs over time scales that are much faster than the radiative decay [25–27]. To spatially address single nanostructures for optical investigation and make it easier to re-locate them for systematic studies ~ 1 μm sized apertures are fabricated in the opaque 200nm thick gold layer on the top contact. These apertures are either fabricated using electron beam lithography [28] or by the deposition of polystyrene nanospheres before the deposition of the gold layer. The polystyrene nanospheres act as shadowmasks during the deposition of the gold layer and are mechanically removed after Au deposition to produce circular apertures through which optical spectroscopy measurements can be performed. A scanning electron microscopy image of a typical aperture fabricated in this way is presented in Figure 1b. Clearly, a circular hole with a diameter of ~ 1 μm can be seen in the gold layer within which the semitransparent Ti contact fixes the surface potential while facilitating optical measurements.

The setup used for the pump-probe experiments with photocurrent readout is presented schematically in Figure 2a. Starting with a 150 fs duration pulse from a tunable Ti:Sa laser (Figure 2a left) two independently tunable pulse trains, the pump and the probe pulses, are derived using a balanced set of two 4f pulse-shapers (Figure 2a bottom). The relative time delay between the two pulse trains is precisely controlled using a delay line (Figure 2a center) that provides a temporal relative tuning range from -300 ps $-$ $+1$ ns with a relative temporal precision < 5 fs. After the pulses are superimposed

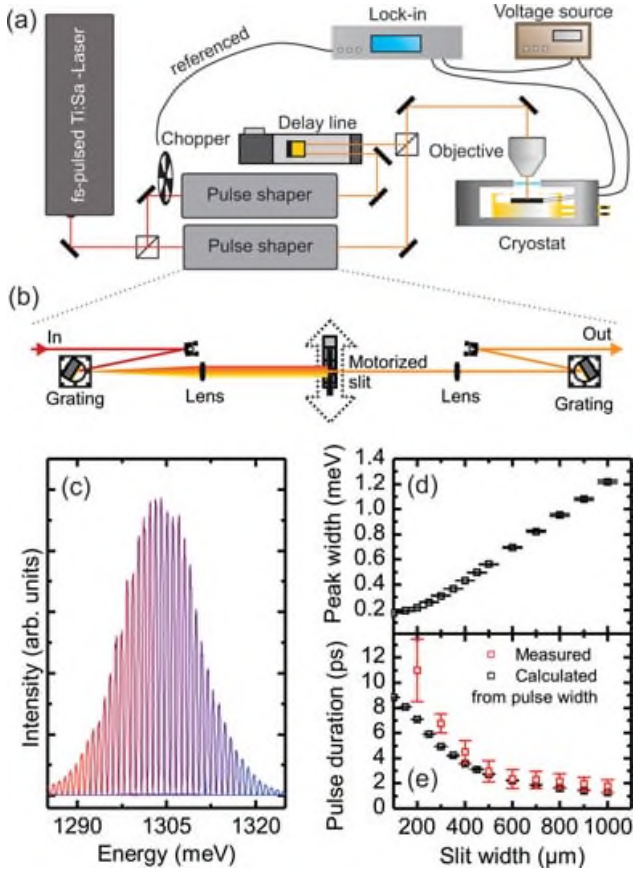

Figure 2 (online color at: www.ann-phys.org) (a) Schematic illustration of the experimental setup used for ultrafast pump-probe spectroscopy with photocurrent readout. (b) Illustration of the 4f pulse shapers. (c) Spectra of the ps pulses obtained from the pulse shaper for different positions of the slit. (d) Spectral width of the output pulses as a function of the slit width. (e) Calculated pulse durations from (d) and measured pulse durations using an autocorellator. The error bars in (c) and the calculated pulse duration in (d) are obtained by fitting the linewidth of the shaped pulses while the error in the measured pulse duration is obtained from temporal autocorrelation.

collinearly they are focused into the cryostat (Figure 2a bottom right) using a reflecting Cassegrain objective. The photocurrent I induced by the probe pulse is measured with a lock-in amplifier that is referenced to the probe pulse using a mechanical chopper. A programmable voltage source connected in series with the lock-in amplifier allows to apply a gate voltage to the sample and, thus, control the internal electric field in the intrinsic region of the devices into which the QDs or QD-molecules are embedded. Blocking and unblocking the pump beam reveals the pump induced change of the probe induced photocurrent ΔI. The quantities I and ΔI can be interpreted as the absorption of the QD nanostructure and its *pump induced change*, respectively [22]. In this representation, a positive value of ΔI corresponds to pump induced absorption whereas negative ΔI corresponds to bleaching. The operating principle of the 4f pulse-shaper is illustrated in Figure 2b. The incident beam (left) is spectrally dispersed using a 1200 l/mm ruled grating and made parallel using an $f = 500$ mm achromatic lens. A tunable slit positioned on a motorized linear stage (center) filters the light in the Fourier plane to transmit spectrally narrow pulses out of the broadband input. To visualize the performance of the pulse shaper its typical spectral output is presented in Figure 2c for different positions of the slit and an incident fs pulse beam centered at 1304 meV. The figure shows the light intensity as a function of photon energy. Clearly sharp peaks at energies ranging from 1285 to 1325 meV can be seen. The envelope of the peaks corresponds to the spectral shape of the input fs-pulses as expected, demonstrating the stable operation of the pulse shaper. The influence of the slit width on the spectral and temporal shape of the pulses is presented in Figures 2d and e. Thereby, Figure 2d presents the fitted spectral pulse width as a function of the slit width. As the figure shows, upon increasing the slit width from 100 to 1000 μm the pulse bandwidth can be tuned from 0.15 meV to 1.2 meV. The temporal pulse duration is investigated in Figure 2e that shows the pulse duration as a function of the slit width. Thereby, the minimum pulse duration calculated from the measured pulse width (Figure 2d) is presented as black squares and the pulse duration measured in the time domain using an autocorellator is shown in red. As the figure shows, for slit widths from 400 to 1000 μm the measured pulse duration corresponds to the calculated pulse duration to an accuracy better than the experimental error. Only for slit widths < 400 μm the measured pulse duration is slightly larger, possibly arising from diffraction effects at the slit.

3 Single quantum dots

In order to investigate the tunneling dynamics of charge carriers from single QDs we performed ultrafast pump-probe experiments with PC readout as discussed in section 2. After we have identified the crystal ground state to neutral exciton transition ($cgs \rightarrow X$) in PL experiments, we continue to trace it in PC experiments that are typically performed with higher applied electric fields. In the next step, for an applied electric field in the PC regime, we fix the energy of the pump pulse to the $cgs \rightarrow X$ transition and measure ΔI as a function of the probe photon energy. An example of typical pump-probe spectra are presented in Figure 3a for $F = 33.3$ kV/cm,

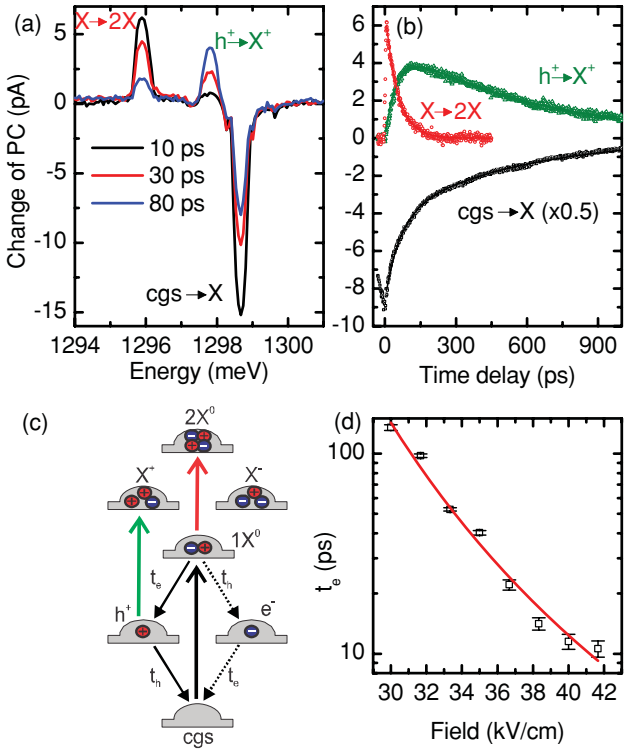

Figure 3 (online color at: www.ann-phys.org) Single quantum dot pump-probe spectroscopy: (a) Change of PC spectra for different time delays between pump and probe. (b) Temporal evolution of ΔI for probing the different transitions from (a). (c) Illustration of the rate equation model of subsequent electron and hole tunneling used for the fits in (b). (d) Dependence of the tunneling time of the electron on the applied electric field. [29]

the pump pulse in resonance with the $cgs \rightarrow X$ transition at 1298.7 meV and three different time delays between pump and probe (Δt) of 10, 30 and 80 ps in black, red and blue, respectively. For all data presented in this paper the lattice temperature of the samples were fixed in the range 4–10 K. For a time delay of 10 ps we observe a pump-induced bleaching at the $cgs \rightarrow X$ transition as shown by the negative signal in Figure 3a and pronounced pump-induced absorption (positive signal at 1295.9 meV, labeled $X \rightarrow 2X$) red shifted by 2.8 meV from the exciton transition. For the larger time delays of 30 and 80 ps between pump and probe pulse, the conditional absorption at 1295.9 meV and the bleaching of the $cgs \rightarrow X$ transition decrease, while a third pump-induced absorption peak appears at 1297.8 meV, labeled $h^+ \rightarrow X^+$ on Figure 3a. The observed pump-probe spectra and their evolution with Δt can be understood with the level scheme depicted schematically in Figure 3c [20–22]. The pump pulse generates an exciton in the QD and, providing that the delay between pump and probe is smaller than the timescales for electron and hole tunneling, the probe pulse can further excite the system to generate a biexciton. This explains the pronounced pump induced absorption peak $X \rightarrow 2X$ at 1295.9 meV in Figure 3a, red-shifted by 2.8 meV from the single neutral exciton transition $cgs \rightarrow X$. As the time delay increases, carriers tunnel out of the QD with the tunneling time of the electron (t_e) with its smaller effective mass being much shorter than that of the hole (t_h) [25, 26]. If the electron tunnels out of the QD, leaving it occupied by a single hole the system exhibits an induced absorption peak at the $h^+ \rightarrow X^+$ transition (peak at 1297.8 meV). To quantitatively analyze electron and hole tunneling, the pump photon energy is fixed to the $cgs \rightarrow X$ transition, while the probe photon energy is tuned to three resonances identified in Figure 3a. For each curve in 3b ΔI is presented as a function of the time delay for probe pulses tuned to the $cgs \rightarrow X$ (black squares), $h^+ \rightarrow X^+$ (green triangles) and $X \rightarrow 2X$ (red circles) transitions, respectively. Fits to the data using a rate equation model of sequential electron and hole tunneling, as illustrated schematically in Figure 3c, are presented as solid lines. In this model, at $t_d = 0$ps the pump pulse generates the initial occupation $N_{1X}(t=0) = N_0$ of the X state and $N_{cgs}(t=0) = 1 - N_0$ of the cgs. Subsequently, electrons and holes tunnel out with the independent rates $1/t_e$ and $1/t_h$, respectively. The analytic solution of the rate equations that describe the time dependent populations and these initial conditions are

$$\begin{aligned} N_X(t) &= N_0 exp\,(-(1/t_e)\,t) \\ N_h(t) &= N_0 \frac{t_h}{t_e - t_h}[exp\,(-t/t_e) - exp\,(-t/t_h)] \\ N_{cgs}(t) &= 1 - N_X(t) - N_h(t) \end{aligned} \qquad (1)$$

Here, N_h is the population of the intermediate states with only one hole in the QD. Probing an optical transition results in a probe-induced photocurrent with an amplitude that is proportional to the difference of the occupations of the final state and the initial state. Since the final state of the $h^+ \rightarrow X^+$ and $X \rightarrow 2X$ transitions are not occupied before probing, the number of the positively charged QDs (N_h) and the X population (N_X) can be directly compared to the temporal scans probing the $h^+ \rightarrow X^+$ and $X \rightarrow 2X$ transitions, respectively. Probing the $cgs \rightarrow X$ transition results in a population inversion ($N_X - N_{cgs}$). As shown by Figure 3b, the model produces good quantitative agreement with the experimental data and allows us to extract tunneling times of $t_e = 53 \pm 1$ps and $t_h = 600 \pm 10$ps. To investigate the dependence of the tunneling times on the applied electric field we performed similar measurements to those presented in

Figure 3a and b for different electric fields in the range $30\,\mathrm{kV/cm} < F < 42\,\mathrm{kV/cm}$. The results of these experiments are summarized in Figure 3d, that shows the extracted tunneling time of the electron as a function of F. Clearly, t_e decreases monotonically from $\sim 135\,\mathrm{ps}$ to $\sim 10\,\mathrm{ps}$ with increasing F and exhibits a clear exponential dependence on the electric field. This behaviour can be fully explained using a WKB treatment of the carrier tunneling rate [30]

$$\Gamma = \frac{16 V_s^2 L}{\pi^2 \hbar^2} \sqrt{\frac{m_s^*}{2|E_s|}} exp\left[-\frac{4\sqrt{2m_s^*}}{3\hbar e F} |E_s|^{\frac{3}{2}} \right] \tag{2}$$

where m_s^* is the effective mass of the particle s (electron or hole), L and V_s are the width and effective depth of the potential well and E_s is the single particle quantization energy. A fit to the experimental data using equation (2) is presented as a red line in Figure 3d and consistently reproduces the experimental data.

4 Quantum dot molecules

QDMs formed from vertically stacking quantum dots exhibit a significant richer spectrum than single dots, due to tunnel coupling of excitonic states that gives rise to anticrossings in optical experiments [12–14, 27, 31, 32]. For the QD-molecule investigated in this study, detailed characterization using PL and PC have been reported in Refs. [27] and [31, 32], respectively. The typical variation of the PL emission with F is presented in Figure 4a. A pronounced anticrossing is seen for electric fields of $F_0 = 23.1\,\mathrm{kV/cm}$ (red shaded peaks). The energy difference between the anticrossing peaks can be fitted with a hyperbolic equation [27]

$$\Delta E = \sqrt{(2V_0)^2 + [ed(F - F_0)]^2} \tag{3}$$

to extract the tunnel coupling strength $2V_0$, the field at which the states anticross F_0 and the equivalent static dipole moment of the indirect exciton ed (d is the distance between the centers of the electron and hole envelope functions). For the anticrossing presented in Figure 4a the values obtained by fitting equation (3) to the data are $F_0 = 23.1 \pm 0.1\,\mathrm{kV/cm}$, $2V_0 = 3.4 \pm 0.1\,\mathrm{meV}$ and $d = 15.3 \pm 0.1\,\mathrm{nm}$. This anticrossing arises from tunnel coupling of two excitonic states where the hole is located in the upper QD and the electron resides either in the lowest energy orbital of the upper (e^0_{ud}) or lower (e^0_{ld}) dot, respectively (c.f. insets of Figure 4a). This anticrossing identifies the involved direct exciton as being the direct exciton in the upper QD.

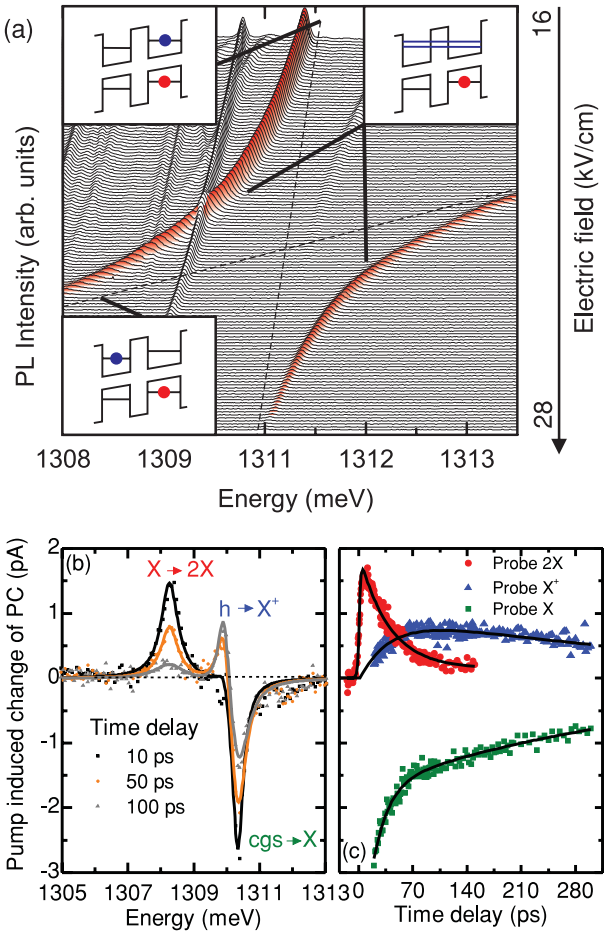

Figure 4 (online color at: www.ann-phys.org) (a) Field dependent PL measurements showing and anticrossing of a direct with an indirect exciton. (b) Change of PC spectra for pumping the direct exciton in the upper dot of the QDM. (c) Temporal evolution of ΔI for probing the different transitions from (b).

As F increases, the PL intensity quenches due to tunneling of the charge carriers out of the molecule such that PC measurements can be performed. The result of a PC measurements that trace the direct exciton in the upper dot as the electric field increases are presented in Figure 5a. The figure shows the PC intensity as a function of F and photon energy in a greyscale representation. Clearly, a series of additional anticrossings can be observed at $F_n = 29.1 \pm 0.1, 29.9 \pm 0.1, 33.1 \pm 0.1$ and $46.2 \pm 0.1\,\mathrm{kV/cm}$. The red lines in Figure 5a show fits to the observed peak positions obtained from a model that includes orbital states in the two dots forming the molecule and including tunnel couplings [31–33]. These additional anticrossings result from the tunnel coupling of different orbitally excited states [31–33], in this case the lowest orbital energy state of the electron in the

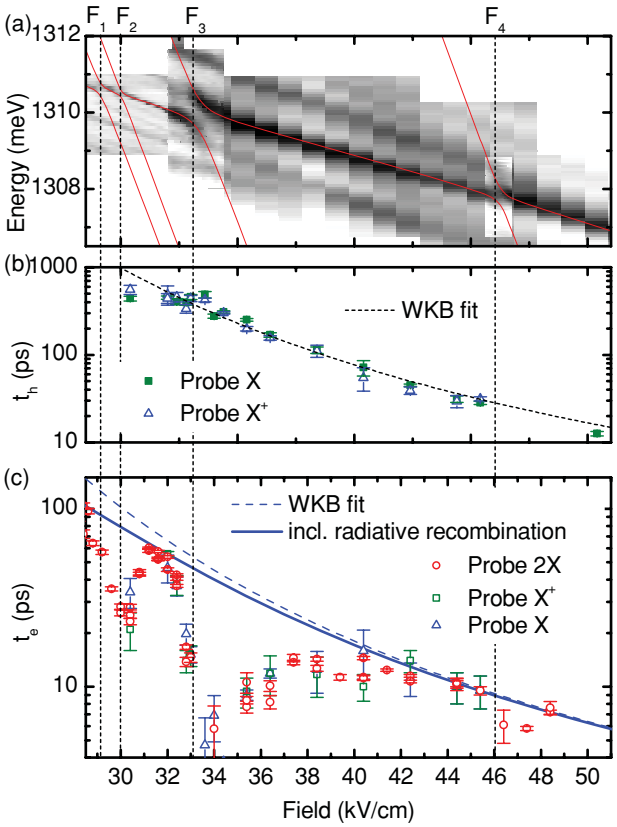

Figure 5 (online color at: www.ann-phys.org) (a) Photocurrent spectra recorded at $T = 10$ K from the molecule. Anticrossings related to tunnel coupling of the electron in the ground state of the upper dot and excited states of the lower dot. (b) Hole and (c) electron tunneling times obtained from probing the transitions identified in Figure 4b. [29]

upper dot e^0_{ud} to different orbitally excited electron states in the lower dot e^n_{ld} (n is the index in increasing energetic order). Taking into account the measured static dipole moment $ed = e \times 15.3 \pm 0.1$ nm of the indirect exciton the difference between the fields where the anticrossings occur F_n can be used to calculate the energy difference between the orbitally excited states [31], e.g. e^3_{ld} lies 15.3 meV higher in energy than e^0_{ld}.

A typical pump probe spectra obtained from the molecule at $F = 32.4 \pm 0.1$ kV/cm and for the pump pulse in resonance with the $cgs \rightarrow X$ transition in the upper dot is presented in Figure 4b. The figure shows ΔI as a function of the probe photon energy for time delays of 10, 50 and 100 ps as black squares, orange circles and gray triangles, respectively. Multi-peak Lorentzian fits are presented as solid lines on the figure. Similar to the single dot experiments presented in the previous section, the pump-induced bleaching of the $cgs \rightarrow X$ transition and the pump-induced absorption of the $h^+ \rightarrow X^+$ and $X \rightarrow 2X$ transitions can be observed. The anticorrelated intensity of $X \rightarrow 2X$ and $h^+ \rightarrow X^+$ resulting from the tunneling of the electron can clearly be observed in Figure 4b as t_d increases from 15 to 100 ps.

To quantitatively analyze electron and hole tunneling, the pump photon energy is fixed to the $cgs \rightarrow X$ transition, while the probe photon energy is tuned to the three resonances identified in Figure 4b. For each curve in 4c ΔI is presented as a function of t_d, for probe pulses tuned to the $cgs \rightarrow X$ (green squares), $h^+ \rightarrow X^+$ (blue triangles) and $X \rightarrow 2X$ (red circles) transitions, respectively. Fits to each set of data using a rate equation model described above show excellent global agreement with all of the measured data and permit the direct, and independent, determination of t_h and t_e in the QD-molecule.

In order to investigate the influence of the couplings presented in Figure 5a on the tunneling dynamics, detailed studies were performed over the range of electric field $29 < F < 51$ kV/cm. The values of t_h obtained with the probe pulse tuned to the $cgs \rightarrow X$ (green squares) and the $h^+ \rightarrow X^+$ (blue triangles) transition are presented in Figure 5b. Similarly, the field dependence of t_e extracted by probing either the $cgs \rightarrow X$, $h^+ \rightarrow X^+$ and $X \rightarrow 2X$ transitions are plotted in Figure 5c. In all cases, the tunneling times obtained by probing the different transitions are in excellent agreement with each other supporting the overall validity of the interpretation and the rate equation model over the whole range of F analyzed here. The hole tunneling time (Figure 5b) monotonically decreases from $t_h = \sim 500$ ps at $F = 30$ kV/cm to $t_h = 12.6$ ps at $F = 50.5$ kV/cm and can be explained by WKB approximation (c.f. equation (2)). A fit to the experimental data is presented as a dashed line in Figure 5b and consistently reproduces the experimental data. The hole tunneling time is well accounted for by WKB theory since the hole tunnels through an approximately triangular potential barrier without any influence of the lower QD.

In marked contrast, the field dependence of t_e (Figure 5c) exhibits significantly richer behavior. Whilst t_e also decreases with F, as expected due to tunneling escape from the QD-molecule, we also observe a series of resonances marked with vertical dashed lines, precisely where the anticrossings of e^0_{ud} with e^1_{ld}, e^2_{ld}, e^3_{ld} and e^4_{ld} occur. The most pronounced resonance occurs at $F_3 = 33.1$ kV/cm where the anticrossing of e^0_{ud} with e^3_{ld} occurs; the strongest of the anticrossings observed in Figure 5a is measured to be $2V_3 = 0.8$ meV. Away from the resonances t_e can be fitted using WKB approximation. A fit to the experimental data taking also into account the radiative recombination is presented in Figure 5c as a

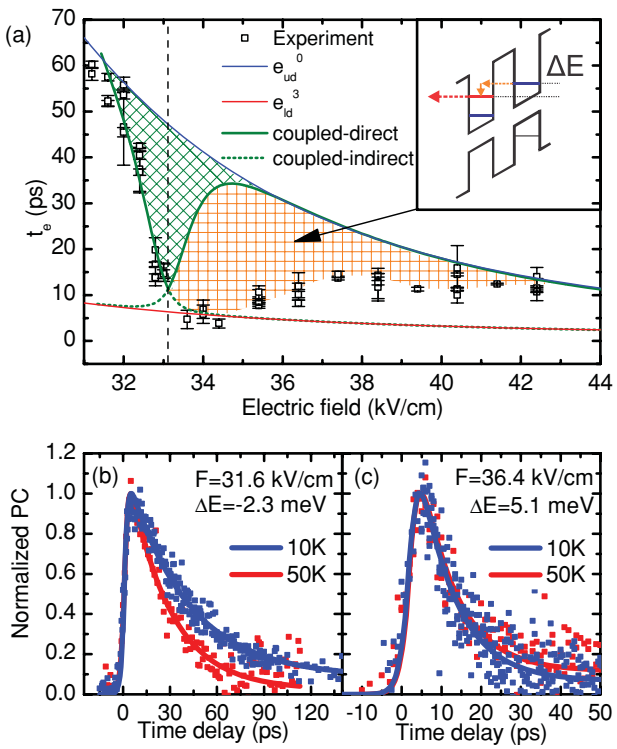

Figure 6 (online color at: www.ann-phys.org) (a) Analysis of the tunneling times from Figure 5c around the tunnel coupling at 33.1 kV/cm. [29] (b-c) Measurements of ΔI as a function of t_d for elevated temperatures of 50 K for a positive (b) and negative (c) detuning of e_{ld}^3 relative to e_{ud}^0.

solid blue line and consistently reproduces the experimental data. The dashed line also presented in Figure 5c is the part of the fit that results from the tunneling alone without radiative recombination. However, at the resonances t_e drastically decreases and even becomes comparable to the laser pulse duration at the couplings at $F_3 = 33.1\,\mathrm{kV/cm}$ and $F_4 = 46.5\,\mathrm{kV/cm}$.

We continue to present a detailed analysis of the ultrafast electron tunneling in the vicinity of the most pronounced anticrossing at $F_3 = 33.1\,\mathrm{kV/cm}$ and show that it contains fingerprints of both elastic resonant tunneling between the two dots forming the molecule and inelastic tunneling with the participation of phonons. The electron tunneling time t_e as a function of F is plotted in Figure 6a on a linear scale, the position of the anticrossing is indicated by the vertical dashed line. In our theoretical analysis we consider tunnel processes according to equation (2) for the two electron levels involved in the anticrossing e_{ud}^0 and e_{ld}^3. The fit of the tunneling time from e_{ud}^0 as obtained in Figure 5c, away from the resonances is plotted in Figure 6a as a blue line. Since the two dots forming the QDM are similar in size and electronic structure, we assume identical confinement potentials for e_{ud}^0 and e_{ld}^0. As discussed above, e_{ld}^3 lies 15.3 meV to higher energy than e_{ld}^0, reducing the effective tunnel barrier. Thus, generically we expect electron tunneling out of the lower dot into the continuum to be faster from e_{ld}^3 compared with e_{ld}^0. Therefore, the tunneling time from e_{ld}^3 can be estimated by keeping the parameters of the fit of the tunneling time from e_{ud} but adding the 15.3 meV that e_{ld}^3 lies higher in energy compared to e_{ld}^0 to the single particle energy. The result of this analysis is plotted as the solid red line in Figure 6a. When the two dots are coupled by tunneling (e.g. for $F = F_3$ - Figure 5a) the Hamiltonian is $\mathbf{H} = \mathbf{H_0} + \mathbf{V_3}$, where $\mathbf{H_0}$ is the Hamiltonian of the detuned system and the coupling term $\mathbf{V_3}$ is measured from the PC data shown in Figure 5a. The effective broadening of the coupled states is then given by the imaginary part of the eigenvalues of the coupled eigenstates $\epsilon_i = E_i - i\Gamma_i$ [32]

$$2\epsilon_{\pm} = \epsilon_{ld^*} + \epsilon_{ud} \pm \sqrt{(\epsilon_{ld^*} - \epsilon_{ud})^2 + 4\,V_3^2} \tag{4}$$

At resonance, the levels are mixed by tunneling and the decay rates of the coupled states exchange character with an intersection at F_3. The corresponding calculated values of t_e are presented as green lines in Figure 6a. For all electric fields we pump the state which is more located in the upper QD (solid green line), resulting in a dip of t_e at F_3. Therefore, the reduction of t_e resulting from the resonant tunnel coupling of e_{ud}^0 to e_{ld}^3 is represented by the diagonal dashed green area in Figure 6a. The theoretical model quantitatively explains the measured values of t_e for $F < F_3$ and $F \gg F_3$. However, pure resonant tunneling would give rise to a much narrower resonance (green dashed area in Figure 6a) than is observed experimentally. In our experiments, the resonance is asymmetrically broadened for $F > F_3$ (orange dashed area). Closer inspection even shows that the shortest time t_e is not observed at F_3 as expected from the theory but shifted by $\Delta F = +1\,\mathrm{kV/cm}$ to 34.1 kV/cm. These clear experimental observations show that an additional mechanism must be active to shorten t_e for $F_3 < F < 41\,\mathrm{kV/cm}$ and produce the asymmetric resonance observed (Figure 6a).

We continue to present evidence that this mechanism is acoustic phonon mediated inelastic inter-dot tunneling into e_{ld}^3 as schematically illustrated in the inset of Figure 6a. The difference between the measured tunneling times t_e and the expected tunneling rates obtained from the model based on equation (4) (orange dashed area in Figure 6a) can be used to calculate an additional tunneling rate. Taking into account the measured static dipole moment $ed = e \times 15.3 \pm 0.1\,\mathrm{nm}$ of the

indirect exciton the additional tunneling rate can be shown to be present up to detunings of +6 meV with a maximum at $+1.7 \pm 0.1$ meV [31]. This characteristic energy scale of a few millielectronvolts corresponds to the energy of acoustic phonons in GaAs with a wavelength comparable to characteristic dimensions in the QD-molecule (width, dot-separation) [15]. Theoretical calculations of the coupling between molecular states and phonons in similar structures (with 12nm separation between the dots) taking into account deformation- and piezoelectric- exciton-phonon coupling reported a spectral density which shows a maximum around +1.4 meV with a rate of 0.3 ps^{-1} [15]. We interpret the additional relaxation channel as reflecting phonon mediated inelastic tunneling between the two dots forming the molecule, as schematically depicted in the inset of Figure 6a. For positive detunings of e^3_{ld} the electron tunnels into e^3_{ld} whilst simultaneously emitting a phonon with an energy equal to the level separation. From there it most likely tunnels out of the excited orbital state of the QDM instead of relaxing to the ground state since the tunneling escape time from the excited state is < 5 ps (see red line in Figure 6a). In contrast, for negative detunings where phonon absorption would be required, such an inelastic tunneling is prohibited by the negligible phonon occupation at the lattice temperature used for the measurements presented here. To test this interpretation we performed measurements of t_e at an elevated temperature of $T = 50$ K where the phonon occupation number increases significantly. Examples of these measurements are presented in Figure 6b for a negative detuning of $\Delta E = -2.3$ meV (phonon absorption) and in (c) for a positive detuning of $\Delta E = 5.1$ meV. The figures present ΔI as a function of the time delay between pump and probe for probing the $X \rightarrow 2X$ transition. Thereby, data recorded at 10 K (50 K) are presented in blue (red). For the case of phonon emission (Figure 6c) t_e remains the same while for the case of phonon absorption (Figure 6b) we observe a strong decrease of t_e from 52 ± 2 ps to 32 ± 3 ps. This behaviour was observed for a series of measurements of positive and negative detunings, strongly supporting the model of phonon-mediated inelastic tunneling to the excited orbital state of the lower dot.

To further elucidate the spin selectivity of the transitions and explore the potential to use ultrafast pulses to prepare and read spin polarized charges we take into account spin selectivity. Therefore, the optical polarization of the two pulses was adjusted to be either co-circular or cross-circular. A typical result of a spin-resolved pump probe spectra is presented in Figure 7a that shows ΔI recorded at $F = 31.2$ kV/cm with the pump pulse fixed to the $cgs \rightarrow X$ transition at 1310.6 meV and the tunable probe pulse delayed by 10 ps. Spectra recorded with cross- and co-circular pump and probe pulses are presented by the red circles and black squares, respectively. For cross-circularly polarized pulses we observe a pump-induced absorption of the $X \rightarrow 2X$ transition and a pump-induced bleaching of the $cgs \rightarrow X$ transition as discussed above. The biexciton absorption is completely absent for the co-circular configuration, an observation attributed to the Pauli spin blockade. In addition, the bleaching of the $cgs \rightarrow X$ transition was found to be twice as strong in the co-circular configuration. While for cross circular polarizations a negative ΔI results from the bleaching of the $cgs \rightarrow X$ only, a co-circular polarized probe pulse may cause stimulated emission of $X \rightarrow cgs$ giving rise to a stronger reduction of ΔI [32] as schematically illustrated in Figure 7a. To study the effect of stimulated emission in more detail, we measure ΔI at the $cgs \rightarrow X$ transition as a function of t_d. The results of these experiments are presented in Figure 7c for cross-circular (red circles) and co-circular (black squares) configurations, respectively. As the figure shows, for time delays longer than 100 ps ΔI is the same for both polarization configurations. This reflects the fact that, after this time the electron has tunneled out of the upper dot where it was photogenerated such that no stimulated emission can occur and bleaching results from the QDM being occupied with a single hole. In contrast,

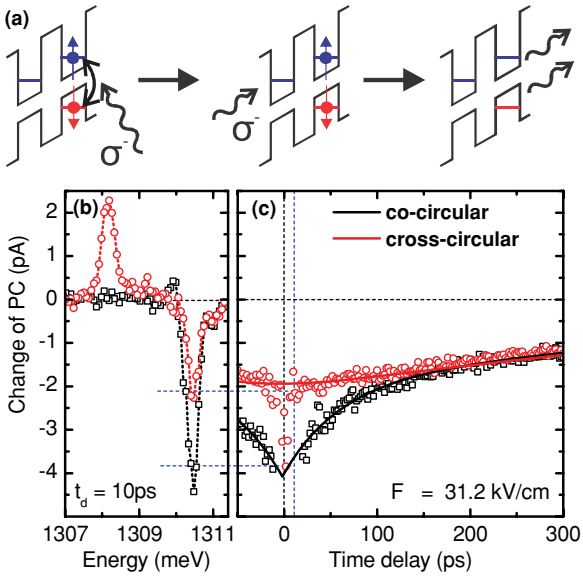

Figure 7 (online color at: www.ann-phys.org) (a) Schematic illustration of stimulated emission in pump-probe experiments. (b) Change of PC spectra at $F = 31.2$ kV/cm for cross- (co-) circular pump and probe as red circles and black squares. (c) Temporal evolution of ΔI for probing the $cgs \rightarrow X$ transition from (b).

for smaller time delays the co-circular configurations exhibits a stronger bleaching due to stimulated emission that occurs only for co-circular polarizations. Fits to the data with the rate equation model taking into account that only the co-polarized configuration can cause stimulated emission results in the solid lines in Figure 7c and quantitatively reproduce the measured data.

In summary, we directly investigated ultrafast tunneling from single and coupled quantum dots using ultrafast pump-probe spectroscopy with PC readout. We determined the tunneling times as a function of F and demonstrated that for single dots the measured tunneling times can be fitted using WKB approximations. Perfect Pauli spin blockade in the $X \rightarrow 2X$ transition was observed, as well as spin-selective stimulated emission. For quantum dot molecules, we showed that t_e exhibits resonances when resonant tunneling can occur between the two dots forming the molecule. In this regime, the tunnel-coupled energy level serves as an intermediate state facilitating electron escape within a few picoseconds. When the orbital states are detuned by a few millielectronvolts, inelastic tunneling involving the emission of acoustic phonons is found to dominate the charge transfer dynamics. We gratefully acknowledge financial support of the DFG via SFB-631, Nanosystems Initiative Munich and the Emmy Noether Program (H.J.K.) and the EU via SOLID. G.A. thanks the TUM Institute for Advanced Study for support. J.M.V.B. acknowledges the support of CNPq and FAPEMIG. We thank A. J. Ramsay, J.M. Daniels, T. Kuhn and P. Machnikowski for discussions.

Key words. Quantum dot molecules, ultrafast pump-probe spectroscopy, inelastic tunneling, tunnel coupling.

References

[1] T. A. Fulton, P. L. Gammel, D. J. Bishop, L. N. Dunkleberger, and G. J. Dolan, Phys. Rev. Lett. **63**(Sep), 1307–1310 (1989).

[2] R. Duschl and K. Eberl, Thin Solid Films **380**(1–2), 151–153 (2000).

[3] M. Julliere, Physics Letters A **54**(3), 225–226 (1975).

[4] H. Kroemer Nobel Lecture(Jul) (2000).

[5] L. Esaki Nobel Lecture (1973).

[6] J. Faist, F. Capasso, D. L. Sivco, C. Sirtori, A. L. Hutchinson, and A. Y. Cho, Science **264**(5158), 553–556 (1994).

[7] R. Hanson, L. P. Kouwenhoven, J. R. Petta, S. Tarucha, and L. M. K. Vandersypen, Rev. Mod. Phys. **79**(Oct), 1217–1265 (2007).

[8] M. Kroner, A. O. Govorov, S. Remi, B. Biedermann, S. Seidl, A. Badolato, P. M. Petroff, W. Zhang, R. Barbour, B. D. Gerardot, R. J. Warburton, and K. Karrai NATURE **451**(7176), 311–314 (2008).

[9] C. Latta, F. Haupt, M. Hanl, A. Weichselbaum, M. Claassen, W. Wuester, P. Fallahi, S. Faelt, L. Glazman, J. von Delft, H. E. Tuereci, and A. Imamoglu NATURE **474**(7353), 627–630 (2011).

[10] N. A. J. M. Kleemans, J. van Bree, A. O. Govorov, J. G. Keizer, G. J. Hamhuis, R. Notzel, A. Y. Silov, and P. M. Koenraad NATURE PHYSICS **6**(7), 534–538 (2010).

[11] Q. Xie, A. Madhukar, P. Chen, and N. P. Kobayashi, Phys. Rev. Lett. **75**(Sep), 2542–2545 (1995).

[12] H. J. Krenner, M. Sabathil, E. C. Clark, A. Kress, D. Schuh, M. Bichler, G. Abstreiter, and J. J. Finley, Phys. Rev. Lett. **94**(5), 057402 (2005).

[13] E. Stinaff, M. Scheibner, A. Bracker, I. Ponomarev, V. Korenev, M. Ware, M. Doty, T. Reinecke, and D. Gammon, Science **311**(5761), 636–639 (2006).

[14] A. S. Bracker, M. Scheibner, M. F. Doty, E. A. Stinaff, I. V. Ponomarev, J. C. Kim, L. J. Whitman, T. L. Reinecke, and D. Gammon, Appl. Phys. Lett. **89**(23), 233110 (2006).

[15] K. Gawarecki, M. Pochwała, A. Grodecka-Grad, and P. Machnikowski, Phys. Rev. B **81**(Jun), 245312 (2010).

[16] K. Gawarecki and P. Machnikowski, Phys. Rev. B **85**(Jan), 041305 (2012).

[17] S. De Franceschi, S. Sasaki, J. M. Elzerman, W. G. van der Wiel, S. Tarucha, and L. P. Kouwenhoven, Phys. Rev. Lett. **86**(5), 878–881 (2001).

[18] H. Qin, A. Holleitner, K. Eberl, and R. Blick Phys. Rev. B **64**(24) (2001).

[19] N. Mason, M. J. Biercuk, and C. M. Marcus, Science **303**(5658), 655–658 (2004).

[20] A. J. Ramsay, S. J. Boyle, R. S. Kolodka, J. B. B. Oliveira, J. Skiba-Szymanska, H. Y. Liu, M. Hopkinson, A. M. Fox, and M. S. Skolnick Phys. Rev. Lett. **100**(19) (2008).

[21] S. J. Boyle, A. J. Ramsay, F. Bello, H. Y. Liu, M. Hopkinson, A. M. Fox, and M. S. Skolnick Phys. Rev. B **78**(7) (2008).

[22] M. Zecherle, C. Ruppert, E. C. Clark, G. Abstreiter, J. J. Finley, and M. Betz, Phys Rev B **82**(12), 125314 (2010).

[23] T. M. Godden, S. J. Boyle, A. J. Ramsay, A. M. Fox, and M. S. Skolnick, Applied Physics Letters **97**(6), 061113 (2010).

[24] T. M. Godden, J. H. Quilter, A. J. Ramsay, Y. Wu, P. Brereton, S. J. Boyle, I. J. Luxmoore, J. Puebla-Nunez, A. M. Fox, and M. S. Skolnick, Phys. Rev. Lett. **108**(Jan), 017402 (2012).

[25] P. Fry, J. Finley, L. Wilson, A. Lemaitre, D. Mowbray, M. Skolnick, M. Hopkinson, G. Hill, and J. Clark APPLIED PHYSICS LETTERS **77**(26), 4344–4346 (2000).

[26] R. Oulton, J. J. Finley, A. D. Ashmore, I. S. Gregory, D. J. Mowbray, M. S. Skolnick, M. J. Steer, S. L. Liew, M. A. Migliorato, and A. J. Cullis, Phys. Rev. B **66**(Jul), 045313 (2002).

[27] K. Müller, G. Reithmaier, E. C. Clark, V. Jovanov, M. Bichler, H. J. Krenner, M. Betz, G. Abstreiter, and J. J. Finley, Phys. Rev. B **84**(8), 081302 (2011).

[28] A. Zrenner JOURNAL OF CHEMICAL PHYSICS **112**(18), 7790–7798 (2000).

[29] The error bars result from the fits to the temporal evolution of ΔI with the rate equation model.

[30] J. Villas-Boas, S. Ulloa, and A. Govorov Phys. Rev. Lett. **94**(5) (2005).

[31] K. Müller, A. Bechtold, C. Ruppert, M. Zecherle, G. Reithmaier, M. Bichler, H. J. Krenner, G. Abstreiter, A. W. Holleitner, J. M. Villas-Boas, M. Betz, and J. J. Finley, Phys. Rev. Lett. **108**(May), 197402 (2012).

[32] K. Müller, A. Bechtold, C. Ruppert, C. Hautmann, J. S. Wildmann, T. Kaldewey, M. Bichler, H. J. Krenner, G. Abstreiter, M. Betz, and J. J. Finley, Phys. Rev. B **85**(Jun), 241306 (2012).

[33] M. Scheibner, M. Yakes, A. S. Bracker, I. V. Ponomarev, M. F. Doty, C. S. Hellberg, L. J. Whitman, T. L. Reinecke, and D. Gammon, Nature Physics **4**(4), 291–295 (2008).